IPN Progress Report 42-185 • May 15, 2011

Computational Ghost Imaging for Remote Sensing Applications

Baris I. Erkmen*

Although ghost imaging owes its early popularity to experiments geared towards demonstrating novel physical principles in quantum optics, it has since developed into a viable structured-illumination imaging modality. As the fundamental physical principles that govern ghost imaging are now well-understood in terms of the coherence theory for classical and quantum light, more attention is being devoted to identifying suitable application areas. Here we report on the rigorous analysis of a ghost-imaging remote-sensing architecture that acquires the 2D spatial Fourier transform of the target object (which can be inverted to obtain a conventional image). We determine its image signature, resolution and signal-to-noise ratio in the presence of practical constraints, such as atmospheric turbulence, background radiation, and photodetector noise. We delineate the impact of turbulence on resolution, and discuss speckle correlography as a possible means of mitigation. Our analysis provides key insights into the performance differences between ghost imaging and conventional active imaging, and identifies scenarios in which ghost imaging—theoretically—yields performance superior to conventional active imagers.

I. Introduction

Ghost imaging is a transverse imaging modality which has been receiving much attention owing to a rich interconnection between low-spatial-coherence imaging physics, and signal processing tailored to active computational imaging. The original ghost imaging experiments consisted of two correlated optical beams traversing distinct paths and impinging on two spatially-separated photodetectors [1, 2, 3, 4, 5, 6]: one beam interacts with the target and then impinges on a single-pixel (bucket) detector that provides no spatial resolution, whereas the other beam traverses an independent path and impinges on a scanning pinhole detector or a high-resolution camera (without any interaction with the target). The image is obtained by correlating the output photocurrents from these photodetectors. Figure 1(a) shows a representative block diagram of this experimental

*Communications Architectures and Research Section

The research described in this publication was carried out by the Jet Propulsion Laboratory, California Institute of Technology, under a contract with the National Aeronautics and Space Administration.

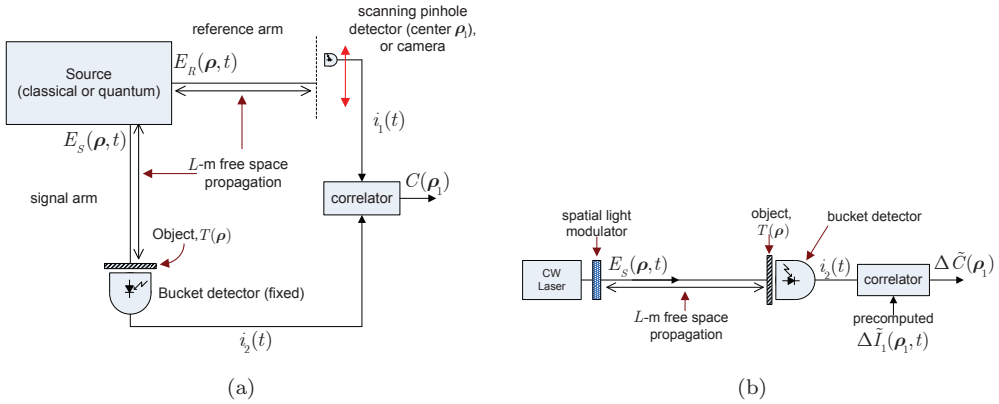

Figure 1. Ghost imaging architectures showing imaging in transmission. (a) In the dual-arm version of ghost imaging, the reference arm is measured with a high-resolution camera (or a scanning pinhole detector) to determine the spatial beam profile (speckle pattern). (b) In computational ghost imaging, the speckle pattern is computed using the transmitter-plane beam profile and paraxial free-space beam propagation theory.

setup. The term "ghost imaging," which was coined soon after the initial experiments were reported, emphasizes the fact that neither photocurrent alone is sufficient to derive the target image, but that by cross correlating the two photocurrents one generates an image of the target. A rich set of ghost imaging experiments have been reported in the scientific literature using both classical and quantum sources of illumination.[1] More recently, a *computational* version of ghost imaging, shown in Figure 1(b), has been proposed [8] and demonstrated [9]. In this configuration of ghost imaging, the measurements obtained from the reference arm (with the high-resolution detector) is replaced by a computational derivation of the measurement-plane intensity profile of the reference-arm beam, using the principles of paraxial free-space propagation. Although its discovery follows a very different path, computational ghost imaging is in fact a structured-illumination imager [10] coupled with computational algorithms to generate the final image. Consequently, the algorithms applied to computational ghost imaging have diversified beyond simple correlation measurements, and now include modern reconstruction algorithms based on compressive sensing [11, 12]. It is feasible to expect further improvements by making use of apriori information regarding the target image.

Although quantum sources—namely, entangled photon pairs—have been shown to have contrast and in some cases signal-to-noise ratio (SNR) advantages over classical sources [6], the low photon-flux of their output limits their applicability to remote sensing. Thus, the focus of our attention in this article is on classical-state ghost imaging, for which bright sources abound. It is worthwhile to begin with a summary of the physics underpinning classical pseudothermal-state ghost imaging. The source beam traverses a

[1] We define a classical source as one whose photodetection statistics can be accurately described using the semiclassical (shot-noise) theory. This is equivalent to having a source state with a proper P-representation as a mixture of coherent states [7]. A quantum source, is one whose photodetection statistics *cannot* be described by the semiclassical theory, i.e., the source state does not have a proper P-representation.

path of length L, and illuminates an object. Because the source has low spatial coherence, i.e., the complex amplitudes of two points on the same transverse plane decorrelate rapidly as the distance between the points exceed a very small fraction of the beam width, the source will project a speckle pattern on the object of interest. The key to ghost imaging is the knowledge of the spatial and temporal variations of this speckle pattern, which is acquired either by measuring the high-resolution image of a reference beam that has the identical speckle pattern (Figure 1(a) version), or by computing the speckle pattern using the knowledge of the transmitted field and the propagation geometry (Figure 1(b) version). The scattered light resulting from the interaction of the illumination and the object is collected with a single-pixel (bucket) detector. The photocurrent—whose fluctuations are ideally proportional to the sum of the fluctuations observed in the transmitter-generated speckles—is then processed to resolve the transverse profile of the object. This signal processing can take on a rather elementary linear form such as cross correlation, or can be more complex and nonlinear, such as L1-norm minimization. Henceforth we refer to the former correlation-based method as *conventional* ghost imaging, as this is the processing utilized in early ghost imaging experiments.

The scientific and engineering community largely now understands the fundamental physical principles that govern ghost imaging using illumination sources that are either classical or quantum. The recent focus has shifted towards identifying applications that can benefit from this imaging modality. For example, ghost imaging has been studied for standoff imaging of the scattering from objects [13], and its performance has been characterized when the imaging is performed through atmospheric turbulence [14, 15]. In this article, we build on this recent literature to analyze, in detail, remote sensing using ghost imaging. Our emphasis here is to highlight the fundamental advantages and disadvantages pertaining to this imaging modality via a rigorous analysis of its performance, and to outline the scenarios in which ghost imaging is desirable over conventional imaging techniques.

Our article is organized as follows. In Section II we begin by introducing the computational ghost imaging architecture that is the focus of our analysis in this article. We derive its image signature and the resolution in Section III. In Section IV we briefly analyze a method by which turbulence-induced resolution degradation can be mitigated. We then derive, in Section V, the signal-to-noise ratio, and we discuss the impact of target-induced speckle. In Section VI we highlight the key conclusions from our analysis and provide a thorough discussion of the fundamental advantages and disadvantages of utilizing computational ghost imaging in remote sensing.

II. Remote Sensing via a Ghost-Imaging Architecture

Consider the remote imaging scenario shown in Figure 2. At the transmitter a continuous-wave (cw) laser with center frequency ω_0—and center wave number $k_0 \equiv \omega_0/c$, where c is the speed of light in vacuum—is spatiotemporally modulated via a spatial light modulator (SLM), and projected onto a distant target. The field leaving the transmitter

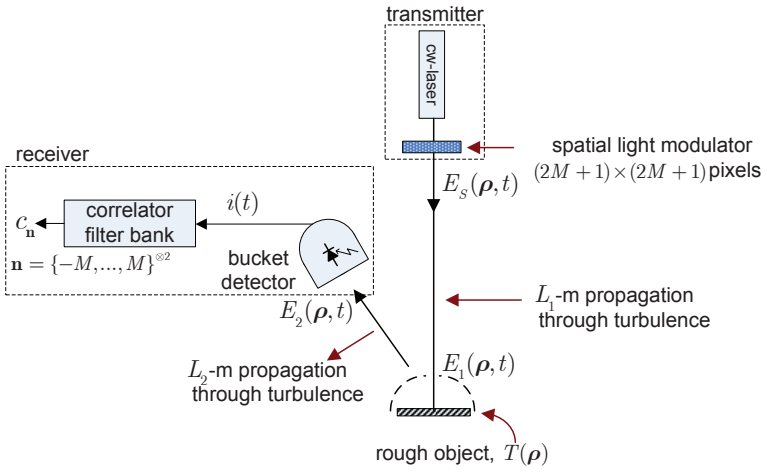

Figure 2. A ghost imaging configuration for remote sensing. The transmitter projects a spatiotemporally modulated laser beam onto a target located L_1 meters away along a path with atmospheric turbulence. The receiver, not necessarily co-located with the transmitter, is L_2 meters away from the target. The target is assumed to be rough on the order of a wavelength, giving rise to diffuse surface scattering and speckle.

pupil, denoted by $E_S(\boldsymbol{\rho},t)e^{-i\omega_0 t}$ where $E_S(\boldsymbol{\rho},t)$ is the baseband envelope in units of $\sqrt{\text{photons/m}^2\text{s}}$, undergoes quasimonochromatic paraxial propagation over a L_1-meter path through atmospheric turbulence. The field incident on the object, whose baseband envelope is denoted by $E_1(\boldsymbol{\rho},t)$, diffusely scatters from the surface of the target that is assumed rough on the order of a wavelength. The surface scattering is therefore modeled as quasi-Lambertian. The ghost-imaging receiver, which is *not* constrained to be co-located with the transmitter, consists of a single-pixel (bucket) detector that simply collects and detects all the power illuminating its aperture. We assume that the receiver is located L_2 meters away from the target, and that the angular extent of the receiver (as seen from the target) is small enough to employ the paraxial approximation to propagate the target-scattered light to the receiver aperture. As the bucket detector does not provide any inherent spatial resolution, the photocurrent must be processed to obtain an image of the object. The processing we consider here is an array of correlation filters that—as we shall see shortly—collectively yield a sampled version of the 2D spatial Fourier transform of the object's mean transverse reflection profile.[2]

In the following subsections we detail the formulation of this remote-sensing scenario. In our analysis we shall include several nonidealities associated with a practical remote-sensing system. First, we presume that background radiation will couple into the receiver aperture, contributing noise to the photocurrent output from the bucket detector. Second, we assume a photodetector with sub-unity detection efficiency[3], nonzero dark

[2]Although we consider a reflection geometry in this article, the results extend to a transmission geometry in a straightforward manner.

[3]We define detection efficiency as the product of losses incurred due to sub-unity transmissivity of optical elements in the front-end of the receiver (e.g., lenses, filters), and the quantum efficiency of the photodetector.

current, non-unity internal gain and associated excess noise (e.g., due to the avalanche process seen in avalanche photodiodes), and nonzero thermal noise (e.g., due to post-detection amplifiers and other electronics).

A. Forward Path (from transmitter to target)

For this discussion let us assume that the transmitted beam is propagating in the positive z direction as shown in Figure 3. Suppose that the SLM at the transmitter is located in the $z = 0$ plane, and consists of a $(2M + 1) \times (2M + 1)$ array of d-meter$\times d$-meter pixels. Because there is little loss in generality, we will assume that the SLM has 100% fill factor, such that it has dimensions $D \times D$, where $D = (2M + 1)d$. We shall assume that the SLM is centered along the optical axis of the transmitter, such that the center of pixel $\mathbf{n} \equiv (n, m)$ is at the transverse coordinate $\boldsymbol{\rho}'_{\mathbf{n}} = (nd, md)$, and it occupies the region

$$\mathcal{A}_{\mathbf{n}} \equiv \left\{ \boldsymbol{\rho}' : \boldsymbol{\rho}' \in \big(nd - d/2, nd + d/2\big] \times \big(md - d/2, md + d/2\big] \right\} \tag{1}$$

on the transverse ($z = 0$) plane, where $n, m = -M, \ldots, M$. We assume that the pixels of the SLM are modulated with circularly-symmetric, independent, identically-distributed, and stationary jointly-Gaussian random processes $f_{\mathbf{n}}(t)$ having the phase-insensitive correlation function

$$R(\tau) \equiv \langle f^*_{\mathbf{n}}(t) f_{\mathbf{n}}(t + \tau) \rangle = e^{-\tau^2/2T_0^2} \tag{2}$$

and the phase-sensitive correlation function $\langle f_{\mathbf{n}}(t) f_{\mathbf{n}}(t + \tau) \rangle = 0$. In equation (2), T_0 is referred to as the coherence time of the modulation.

Suppose that a z-propagating cw laser field with center frequency ω_0, photon flux P (with units photons/s), and a spatially-uniform transverse profile, is incident on the SLM. The baseband envelope of the output field from the SLM is given by

$$E_S(\boldsymbol{\rho}', t) = \sqrt{\frac{P}{D^2}} \sum_{\mathbf{n}} f_{\mathbf{n}}(t) \xi(\boldsymbol{\rho}' - \mathbf{n}d) \tag{3}$$

where

$$\xi(\boldsymbol{\rho}') \equiv \begin{cases} 1, & \boldsymbol{\rho}' \in (-d/2, d/2] \times (-d/2, d/2] \\ 0, & \text{otherwise} \end{cases} \tag{4}$$

is an indicator function corresponding to one pixel on the $z = 0$ plane.

Along the path to the target, $E_S(\boldsymbol{\rho}', t)$ undergoes quasimonochromatic paraxial propagation through atmospheric turbulence. The Extended Huygens-Fresnel principle is used to determine the baseband envelope of the field at the object plane $z = L_1$, denoted by $E_1(\boldsymbol{\rho}, t)$ and given by [16, 17, 18]

$$E_1(\boldsymbol{\rho}, t) = \int E_S(\boldsymbol{\rho}', t - L_1/c) h_{\mathrm{FS}}(\boldsymbol{\rho} - \boldsymbol{\rho}'; L_1) e^{\psi(\boldsymbol{\rho}, \boldsymbol{\rho}')} \mathrm{d}\boldsymbol{\rho}' \tag{5}$$

For the purposes of our analysis, all of these efficiency factors can be combined into one parameter which we refer to as the detection efficiency.

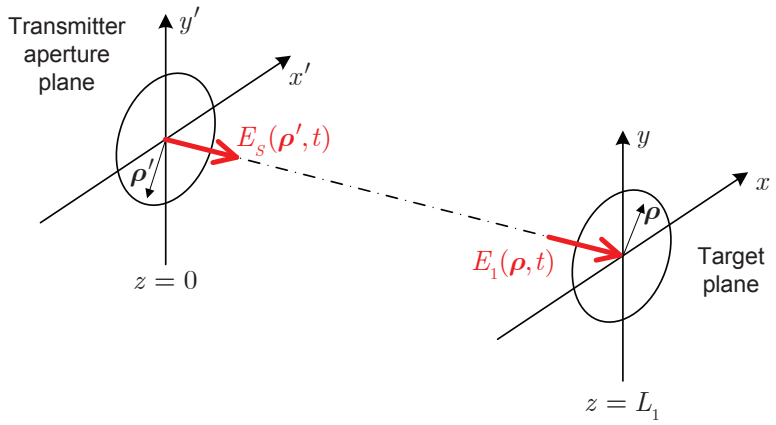

Figure 3. The paraxial propagation geometry for the transmitted beam.

where $h_{\mathrm{FS}}(\boldsymbol{\rho}; L)$ is the Huygens-Fresnel free-space (i.e., vacuum) propagation Green's function

$$h_{\mathrm{FS}}(\boldsymbol{\rho}; L) \equiv \frac{k_0 e^{ik_0 L}}{i2\pi L} e^{i\frac{k_0}{2L}|\boldsymbol{\rho}|^2} \tag{6}$$

and $\psi(\boldsymbol{\rho}, \boldsymbol{\rho}')$ is a *complex-valued* Gaussian random field denoting the phase and amplitude fluctuations due to atmospheric turbulence seen at $\boldsymbol{\rho}$ on the $z = L_1$ plane, given a point source at $\boldsymbol{\rho}'$ on the $z = 0$ plane. In the weak-fluctuation regime, the real and imaginary parts of $\psi(\boldsymbol{\rho}, \boldsymbol{\rho}')$—typically denoted with $\chi(\boldsymbol{\rho}, \boldsymbol{\rho}')$ and $\phi(\boldsymbol{\rho}', \boldsymbol{\rho})$ respectively—are jointly Gaussian random fields, and within the regime of validity of Kolmogorov-spectrum turbulence the two-source spherical-wave wave structure function for ψ becomes [17]

$$\begin{aligned} D_{\psi,\psi}(\boldsymbol{\rho}, \boldsymbol{\rho}') &\equiv \left\langle \left| \psi(\boldsymbol{\rho}_1, \boldsymbol{\rho}_1') - \psi(\boldsymbol{\rho}_1 + \boldsymbol{\rho}, \boldsymbol{\rho}_1' + \boldsymbol{\rho}') \right|^2 \right\rangle \\ &= 2.914 k_0^2 L_1 \int_0^1 C_{n,T}^2(sL_1) |\boldsymbol{\rho}'(1-s) + \boldsymbol{\rho} s|^{5/3} \mathrm{d}s \end{aligned} \tag{7}$$

where $C_{n,T}^2(z)$ is the turbulence strength profile along the transmitter-to-target path. In the preceding formulation we have implicitly assumed a *frozen atmosphere* model, i.e., we have assumed that the temporal window of interest (the integration time at the receiver) is significantly shorter than the coherence time of the turbulent eddies that give rise to the $\psi(\boldsymbol{\rho}, \boldsymbol{\rho}')$ term, such that the time-dependence of the fluctuations can be neglected.

Substituting equation (3) into equation (5), and assuming that L_1 is far enough into the far-field such that the quadratic phase factors encountered in equation (5) can be safely neglected, we find that the field incident on the target is given by

$$E_1(\boldsymbol{\rho}, t) = \sqrt{\frac{P}{D^2}} \frac{k_0 d^2}{i2\pi L_1} \Xi(k_0 \boldsymbol{\rho} / L_1) \sum_{\mathbf{n}} f_{\mathbf{n}}(t - L_1/c) e^{\psi(\boldsymbol{\rho}, \mathbf{n}d)} e^{-i\frac{k_0}{L_1}\boldsymbol{\rho}\cdot\mathbf{n}d} \tag{8}$$

where

$$\Xi(\mathbf{k}) \equiv \frac{\sin(k_x d/2)}{k_x d/2} \frac{\sin(k_y d/2)}{k_y d/2} \tag{9}$$

and $\mathbf{k} \equiv (k_x, k_y)$. In arriving at equation (8) we have made the additional assumption that d is much smaller than the transmitter-plane coherence length of the atmosphere, denoted

henceforth as ρ_0.[4] Given that SLM pixels are typically tens of micrometers, and ρ_0 in the weak turbulence regime is on the order of centimeters [17, 18], this approximation is likely to hold in most imaging scenarios.

B. Return Path (from target to receiver)

The incident field $E_1(\boldsymbol{\rho}, t)e^{-i\omega_0 t}$ scatters off of the stationary target surface, denoted by $T(\boldsymbol{\rho})$. We assume that the surface roughness of the object is on the order of a wavelength, giving rise to quasi-Lambertian scattering, whose statistics we model as a zero-mean Gaussian random field $T(\boldsymbol{\rho})$, with the second-order moments

$$\langle T^*(\boldsymbol{\rho}_1)T(\boldsymbol{\rho}_2)\rangle = \frac{\lambda_0^2}{\pi}\mathcal{T}(\boldsymbol{\rho}_1)\delta(\boldsymbol{\rho}_1 - \boldsymbol{\rho}_2) \tag{10}$$

and $\langle T(\boldsymbol{\rho}_1)T(\boldsymbol{\rho}_2)\rangle = 0$. Here $\lambda_0 \equiv 2\pi/k_0$ is the center wavelength of the illumination, and $\mathcal{T}(\boldsymbol{\rho})$ is the (ensemble-averaged) transverse profile of the target that we would like to image.[5] The baseband envelope of the field at the receiver aperture—the bucket detector shown in Figure 2—can be evaluated using, once again, the Extended Huygens-Fresnel principle

$$E_2(\boldsymbol{\rho}, t) = \int T(\boldsymbol{\rho}')\, E_1(\boldsymbol{\rho}', t - L_2/c)h_{\mathrm{FS}}(\boldsymbol{\rho} - \boldsymbol{\rho}'; L_2)e^{\psi_R(\boldsymbol{\rho},\boldsymbol{\rho}')}\mathrm{d}\boldsymbol{\rho}'\,. \tag{11}$$

Here ψ_R is the turbulence-induced complex phase perturbation on the return path, with a structure function given by the same form in equation (7), but with $C_{n,R}^2(z)$ replacing $C_{n,T}^2(z)$ as the turbulence profile on the return path. Note that, because we do not assume that the receiver is co-located with the transmitter, the turbulence profile on the target return path may be significantly different than that on the forward path.

The measurement at the receiver is a $(2M+1)^2$-element filter bank yielding the outputs[6]

$$c_{\mathbf{n}} = \frac{1}{T}\int_{-T/2}^{T/2} g_{\mathbf{n}}(t)i(t)\mathrm{d}t \tag{12}$$

where $i(t)$ is the photocurrent (reported here in units of electrons/s) generated by the bucket detector, and T is the integration time. The filter impulse responses are given by

$$g_{\mathbf{n}}(t) \equiv f_{\mathbf{0}}^*(t)f_{\mathbf{n}}(t) - \langle f_{\mathbf{0}}^*(t)f_{\mathbf{n}}(t)\rangle\,. \tag{13}$$

Our motivation for choosing these filters will become apparent in Section III where we derive the image signature.

---

[4] We define $\rho_0 \equiv \left(2.914k_0^2 L_1 \int_0^1 C_{n,T}^2(sL_1)(1-s)^{5/3}\mathrm{d}s\right)^{-3/5}$, i.e., ρ_0 is the displacement at which $D_{\psi,\psi}(\mathbf{0}, \boldsymbol{\rho})$ equals unity.

[5] Our choice of the denominator π in the expression above is to ensure that with $\mathcal{T}(\boldsymbol{\rho}) = 1$, the correlation function is consistent with that of a Lambertian scatterer [19].

[6] As we shall see in Section III, the number of measurements can be reduced by a factor of two due to the conjugate symmetry between the $c_{\mathbf{n}}$ and $c_{-\mathbf{n}}$ measurements. However, we shall not dwell on this further here.

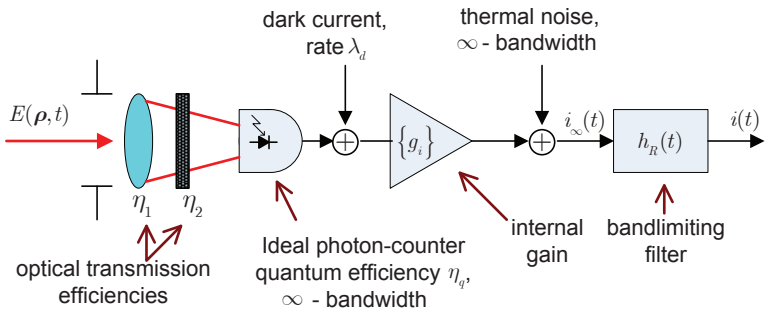

Figure 4. The photodetection model used in the analysis of the ghost imaging receiver. The detection efficiency is given by $\eta < 1$ (here equal to $\eta = \eta_1\eta_2\eta_q$). The photodetector is assumed to have dark current with rate λ_d. The internal gain of the detector is random with mean $\langle g_i \rangle = G$, and second moment $\langle g_i^2 \rangle = FG$, where $F > 1$ is the excess noise factor (non-random gain can be modeled by setting $F = 1$). Infinite-bandwidth thermal noise with spectrum N_T is added to represent noise from post-detection electronics. The overall bandwidth of the detector plus amplifier chain is represented with a linear time-invariant filter $h_R(t)$. The output from this filter is the observed photocurrent $i(t)$.

In our analysis we include the impact of several noise sources seen in nonideal photodetectors, as shown in the Figure 4 model. In particular, we allow a sub-unity detection efficiency η, dark current with rate λ_d (normalized to have units electrons/s), internal random gain with mean value G and excess noise factor F,[7] and zero-mean thermal noise with constant spectrum N_T (reported in units of electrons^2/s) over the bandwidth of the band-limiting filter $h_R(t)$. The observed photocurrent $i(t)$ is therefore a random process given by

$$i(t) = \int h_R(t-\tau) i_\infty(\tau) \mathrm{d}\tau \tag{14}$$

where $i_\infty(t)$ represents an infinite-bandwidth (random) photocurrent, and the finite bandwidth of the receiver is modeled via $h_R(t)$. We will see in Section V that AC coupling the photocurrent $i(t)$ improves noise rejection, and therefore, we will assume that $h_R(t)$ includes a DC notch. Furthermore, for analytic convenience, we shall assume that the composite baseband frequency response of the photodetectors and their AC-coupling is given by the difference of two Gaussian functions

$$H_R(\omega) = \mathcal{F}[h_R(t)] = e^{-2\omega^2/\omega_R^2} - e^{-2\omega^2/\omega_N^2} \tag{15}$$

where ω_R is the baseband bandwidth of the detector, $\omega_N \ll \omega_R$ is the stopband bandwidth of the AC-coupling notch around $\omega = 0$, and $\mathcal{F}[h_R(t)]$ denotes the Fourier transform of the composite filter's impulse response, $h_R(t)$. In order to minimize suppression of the baseband photocurrent fluctuations, $\omega_N T_0 \ll 1$ will be assumed in all that follows.

Using the semiclassical theory for photodetection,[8] $i_\infty(t)$ can be modeled as a random

[7] The excess noise factor F is the ratio of the second moment of the gain to the square of the mean.

[8] Because our focus in this article is strictly on classical fields, we shall rely on the semiclassical theory of photodetection, which yields quantitatively equivalent results to a full quantum treatment of the measurement [5, 7].

process with conditional mean

$$\langle i_\infty(t)|P(t)\rangle = G\eta P(t) + \lambda_d \tag{16}$$

and conditional covariance

$$\langle \Delta i(t_1)\Delta i(t_2)|P(\cdot)\rangle = \Big[FG^2\big(\eta P(t_1) + \lambda_d\big) + N_T\Big]\delta(t_2 - t_1) \tag{17}$$

where $\Delta i(t) = i(t) - \langle i(t)|P(t)\rangle$, and $P(t)$ is the photon flux incident at the receiver aperture $\mathcal{A}_R$, given by

$$P(t) = \int_{\mathcal{A}_R} |E_2(\boldsymbol{\rho}, t) + E_B(\boldsymbol{\rho}, t)|^2 \mathrm{d}\boldsymbol{\rho}\,. \tag{18}$$

In equation (18) we have represented the field incident on the receiver aperture as the superposition of the desired signal field $E_2(\boldsymbol{\rho}, t)$ and a background field, $E_B(\boldsymbol{\rho}, t)$. We shall model the latter as a zero-mean Gaussian random field with the nonzero phase-insensitive correlation function

$$\langle E_B^*(\boldsymbol{\rho}_1, t_1)E_B(\boldsymbol{\rho}_2, t_2)\rangle = I_B K_B(\boldsymbol{\rho}_2 - \boldsymbol{\rho}_1)R_B(t_2 - t_1) \tag{19}$$

where I_B is the uniform mean photon irradiance (with units of photons/m^{2}s), $K_B(\boldsymbol{\rho})$ is the spatial correlation function with width on the order of the center wavelength λ_0, and $R_B(\tau)$ is the temporal correlation function with coherence time much shorter than both the integration time of the photodetector and the modulation rate, T_0, of the source. The source of this background radiation in remote sensing applications during the daytime is primarily diffusely-scattered sunlight, which results in a background sky radiance for sensors looking up towards the sky, and a background upwelling radiance for sensors looking down at the Earth (terrestrial imaging systems may experience a combination of these two background sources) [20, 21].[9]

III. Image Signature

At this juncture we have defined all of the necessary components to derive the mean image signature of this remote-sensing instrument. In the following analysis, we are going to neglect the transmitter-to-receiver propagation time delay equal to $(L_1 + L_2)/c$, to reduce the notation clutter. This can be added in later, by simply shifting the time index at the receiver by this propagation delay. Using equation (12), we can write the mean values of the outputs from the receiver filters as

$$\langle c_{\mathbf{n}}\rangle = \frac{1}{T}\int_{-T/2}^{T/2}\int_{-\infty}^{\infty} h_R(t-\tau)\langle g_{\mathbf{n}}(t)i_\infty(\tau)\rangle \mathrm{d}\tau\mathrm{d}t\,. \tag{20}$$

Thus, the key step to determining $\langle c_{\mathbf{n}}\rangle$ is evaluating

$$\langle g_{\mathbf{n}}(t)i_\infty(\tau)\rangle = \eta G\Big\langle g_{\mathbf{n}}(t)\int_{\mathcal{A}_R}\big\langle |E_2(\boldsymbol{\rho}, \tau)|^2|\{f_{\mathbf{n}}\}\big\rangle \mathrm{d}\boldsymbol{\rho}\Big\rangle \tag{21}$$

[9] In our analysis we are neglecting any coherent reflections from layers in the atmosphere (or the space-atmosphere boundary) that may couple a fraction of the transmitter-modulated field into the receiver. Such noise would result in a non-zero background in the image signature and degrade the signal-to-noise ratio.

where we have used $\{f_{\mathbf{n}}\}$ as the shorthand notation for the set of all modulation functions for $t \in [-T/2, T/2]$. The right-hand side of the expression above is obtained by the judicious use of the law of iterated expectations, the conditional mean from equation (16), and the observation that $\langle g_{\mathbf{n}}(t)\rangle = 0$. Expanding $E_2(\boldsymbol{\rho}, \tau)$ using equation (11), and utilizing equation (10) along with the fact that the fluctuations of $E_1(\boldsymbol{\rho}, t)$ and those induced by the target $T(\boldsymbol{\rho})$ are independent, we obtain

$$\int_{\mathcal{A}_R} \big\langle |E_2(\boldsymbol{\rho}, \tau)|^2 | \{f_{\mathbf{n}}\}\big\rangle \mathrm{d}\boldsymbol{\rho} = \frac{1}{\pi L_2^2} \left(\int_{\mathcal{A}_R} \langle e^{2\chi(\boldsymbol{\rho}', \boldsymbol{\rho})}\rangle \mathrm{d}\boldsymbol{\rho} \right) \int_{\mathbb{R}^2} \mathcal{T}(\boldsymbol{\rho}') |\Xi(k_0 \boldsymbol{\rho}'/L_1)|^2 \big\langle |E_1(\boldsymbol{\rho}', \tau)|^2 | \{f_{\mathbf{n}}\}\big\rangle \mathrm{d}\boldsymbol{\rho}' \,. \quad (22)$$

The integral in the parenthesis above is equal to A_R because $\langle \exp\{2\chi(\boldsymbol{\rho}', \boldsymbol{\rho})\}\rangle = 1$ for clear-air turbulence. This shows that the value of $\langle c_{\mathbf{n}}\rangle$ is *unaffected* by turbulence on the return path from the target.

To simplify equation (22) we assume that $\mathcal{T}(\boldsymbol{\rho}')|\Xi(k_0\boldsymbol{\rho}'/L_1)|^2 \approx \mathcal{T}(\boldsymbol{\rho}')$, i.e., that the target of interest is well within the area of illumination. Then, substituting equation (22) into equation (20), we find that $\langle g_{\mathbf{n}}(t)|E_1(\boldsymbol{\rho}', \tau)|^2\rangle$ must be evaluated, which is straightforward to do using equation (8), and noting that

$$\langle g_{\mathbf{n}}(t) f^*_{\mathbf{n}'}(\tau) f_{\mathbf{m}'}(\tau)\rangle = |R(t-\tau)|^2 \delta_{\mathbf{0},\mathbf{m}'} \delta_{\mathbf{n},\mathbf{n}'} \quad (23)$$

where $R(\tau)$ is defined in equation (2), and $\delta_{\mathbf{n},\mathbf{m}} = 1$ for $\mathbf{n} = \mathbf{m}$, but 0 otherwise. Substituting the result back into equation (20), we arrive at our final answer

$$\langle c_{\mathbf{n}}\rangle = \frac{\Omega_R}{2\pi} \times 2\eta G P \frac{d^2}{D^2} \frac{d^2}{\lambda_0^2 L_1^2} \times \frac{1}{\sqrt{1 + \frac{8}{\omega_R^2 T_0^2}}} \times \widetilde{\mathcal{T}}_{\mathbf{n}} e^{-D(\mathbf{n})/2} \quad (24)$$

where Ω_R is the solid angle subtended by the receiver aperture as seen from the target,

$$\widetilde{\mathcal{T}}_{\mathbf{n}} \equiv \int \mathcal{T}(\boldsymbol{\rho}) e^{i2\pi d \mathbf{n}\cdot\boldsymbol{\rho}/\lambda_0 L_1} \mathrm{d}\boldsymbol{\rho} \quad (25)$$

is the sampled 2D spatial Fourier transform of the object image, and

$$D(\mathbf{n}) \equiv \exp\left\{ -\frac{|\mathbf{n}|^{5/3}}{(\rho_0/d)^{5/3}} \right\} \quad (26)$$

is the single-source wave structure function of the atmosphere, with ρ_0 denoting the transmitter-plane coherence length. From this expression we see that, in the absence of turbulence ($\rho_0 \to \infty$), the receiver reconstructs the 2D Fourier transform of the object's transverse profile, sampled at intervals $d/(\lambda L_1)$. Using time-frequency Nyquist relations we can conclude that the sampling period would result in aliasing of the target $\mathcal{T}(\boldsymbol{\rho})$ outside of the radius $\lambda L_1/d$. However, because we have already assumed that $\mathcal{T}(\boldsymbol{\rho}')|\Xi(k_0\boldsymbol{\rho}'/L_1)|^2 \approx \mathcal{T}(\boldsymbol{\rho}')$, the target is confined well-within this radius, consequently, aliasing is negligible.

Let us define the diffraction-limited resolution as the inverse of the highest sampled spatial frequency of the target image, i.e.,

$$r_{\mathrm{d}} \equiv \frac{\lambda_0 L_1}{Md} = \frac{2M+1}{2M} \frac{2\lambda_0 L_1}{D} \approx \frac{2\lambda_0 L_1}{D} \quad (27)$$

where the last approximation follows from $M \gg 1$. From equation (24), we find that, in the presence of turbulence, the *forward*-path turbulence results in a multiplicative, exponentially-decaying attenuation in spatial frequency, with the e^{-1} attenuation occurring at $M_{\mathrm{t}} = 2^{3/5}\rho_0/d$. Then, the resolution in the presence of turbulence can be written as

$$r \equiv \max\left(\frac{\lambda_0 L_1}{Md}, \frac{\lambda_0 L_1}{M_{\mathrm{t}} d}\right) \approx \frac{2\lambda_0 L_1}{\min\left(D, 2^{8/5}\rho_0\right)}. \tag{28}$$

Therefore, if the transmitter aperture width exceeds the transmitter-plane atmospheric coherence length ρ_0, the image resolution becomes turbulence limited, and it saturates at $r_{\mathrm{t}} = \lambda_0 L_1/(2^{3/5}\rho_0)$. Recall that the image resolution in classical free-space (i.e., vacuum) ghost imaging is proportional to the size of the speckles at the object plane [6], which is inversely proportional to the source diameter in far-field imaging. Thus, in the absence of turbulence, the larger the transmitter aperture, the higher the image resolution. However, this relation no longer holds when turbulence is present in front of the transmitter aperture. In particular, when the transmitter aperture exceeds the atmospheric coherence diameter, the far-field speckle size becomes limited by the atmospheric coherence length, and this results in the turbulence-limited saturation seen in equation (28).

The transition of resolution from the diffraction-limited regime to the turbulence-limited regime can be shown analytically when Gaussian functions are employed to approximate the last term in equation (24). In particular, we write

$$\widetilde{\mathcal{T}}_{\mathbf{n}} e^{-|\mathbf{n}|^{5/3}/2(\rho_0/d)^{5/3}} \times \mathrm{sqr}\left(\mathbf{n}, M\right) \approx \widetilde{\mathcal{T}}_{\mathbf{n}} e^{-|\mathbf{n}d|^2/2\rho_0^2} e^{-|\mathbf{n}d|^2/2(Md)^2} \tag{29}$$

where $\mathrm{sqr}(\mathbf{n}, M) = 1$ if $n, m \in \{-M, \ldots, M\}$, and 0 otherwise. Next, by replacing $\mathbf{n}d$ with a continuous spatial-frequency variable $\lambda_0 L_1 \mathbf{f}$, and inverse Fourier transforming the function, we find that the resolution of the image is given by

$$r = \frac{2\lambda_0 L_1}{D}\sqrt{1 + \frac{D^2}{4\rho_0^2}} \tag{30}$$

which is in agreement with earlier derivations of the resolution of ghost imaging over horizontal-path turbulence [15]. The transition between the two regimes is shown in Figure 5.

IV. Speckle Reduction via Correlography

As we have shown in the previous section, the ghost imaging mean signature becomes limited by turbulence when the transmitter-plane atmospheric coherence length is smaller than the transmitter aperture diameter. This limitation can be overcome by well-known speckle mitigation techniques, which are applicable when the object of interest lies in a single isoplanatic patch [17, 18]. Here we shall briefly describe one such technique. Let us begin by considering the *short exposure* image signature, wherein the integration time T is chosen to be much shorter than the atmospheric coherence time, such that independent realizations of the turbulence-induced random complex phase terms are not averaged

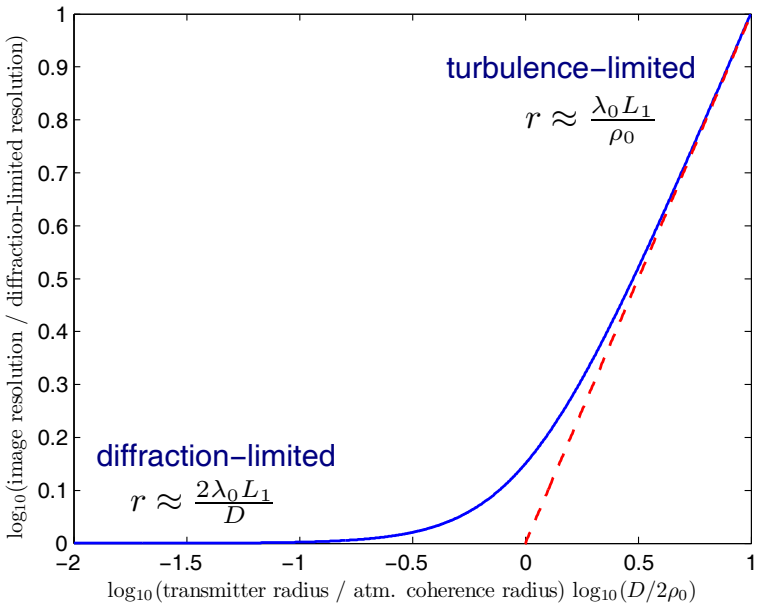

Figure 5. The plot shows the transition of ghost-image resolution from the diffraction-limited regime to the turbulence-limited regime as the aperture size increases.

over.[10] Using equations (22) and (8), the short-exposure image can be expressed as

$$\langle c_{\mathbf{n}}\rangle_{\mathrm{s}} = \frac{1}{\pi L_2^2}\left(\int_{\mathcal{A}_R} e^{2\chi(\boldsymbol{\rho}',\boldsymbol{\rho})}\mathrm{d}\boldsymbol{\rho}\right)\int \mathcal{T}(\boldsymbol{\rho}')e^{\psi^*(\boldsymbol{\rho}',\mathbf{0})+\psi(\boldsymbol{\rho}',\mathbf{n}d)}e^{i\frac{k_0 d}{L_1}\boldsymbol{\rho}'\cdot\mathbf{n}}\mathrm{d}\boldsymbol{\rho}'\,. \tag{31}$$

Assuming that the coherence diameter of the turbulence on the return path is much smaller than the receiver aperture diameter, the integral over the return-path turbulence can be approximated by its mean value A_R (we know from the previous section that this relation holds with equality in the long-exposure case). Now suppose, in addition, that the object lies in a single isoplanatic patch, such that

$$\int \mathcal{T}(\boldsymbol{\rho}')e^{\psi^*(\boldsymbol{\rho}',\mathbf{0})+\psi(\boldsymbol{\rho}',\mathbf{n}d)}e^{i\frac{k_0 d}{L_1}\boldsymbol{\rho}'\cdot\mathbf{n}}\mathrm{d}\boldsymbol{\rho}' \approx e^{\psi^*(\mathbf{0},\mathbf{0})+\psi(\mathbf{0},\mathbf{n}d)}\widetilde{\mathcal{T}}_{\mathbf{n}} \tag{32}$$

is a valid approximation. If the receiver evaluates $|\langle c_{\mathbf{n}}\rangle_{\mathrm{s}}|^2$ in each of these short exposures, then the turbulence-averaged image becomes

$$\langle|\langle c_{\mathbf{n}}\rangle_s|^2\rangle = \left(\frac{\Omega_R}{2\pi}\times 2\eta GP\frac{d^2}{D^2}\frac{d^2}{\lambda_0^2 L_1^2}\times\frac{1}{\sqrt{1+\frac{8}{\omega_R^2 T_0^2}}}\right)^2 e^{4K_{\chi,\chi}(\mathbf{0},\mathbf{n}d)}|\widetilde{\mathcal{T}}_{\mathbf{n}}|^2 \tag{33}$$

where $K_{\chi,\chi}(\boldsymbol{\rho},\boldsymbol{\rho}')$ is the covariance function of the log-amplitude turbulence fluctuations. Because these fluctuations are often assumed to be negligible compared to the fluctuations in the phase, $\exp[4K_{\chi,\chi}(\mathbf{0},\mathbf{n}d)]\approx 1$. In other words, as is common in techniques tailored

[10] Given that the atmospheric coherence time is typically longer than a millisecond, and SLM's have modulation bandwidths that are several MHz, correlations can be taken nominally over thousands of modulation symbols before the state of turbulence has significantly changed.

to mitigate speckle noise, it is possible to resolve $|\widetilde{\mathcal{T}}_{\mathbf{n}}|^2$ at approximately the diffraction limit, but only at the expense of the phase information in $\widetilde{\mathcal{T}}_{\mathbf{n}}$. Despite the lack of phase information from the direct measurements, however, all hope is not lost in reconstructing $\mathcal{T}(\boldsymbol{\rho})$. In particular, $\widetilde{\mathcal{T}}_{\mathbf{n}}$ is the (complex-valued) 2D Fourier transform of a *nonnegative* function, and therefore its phase is constrained. Iterative phase retrieval algorithms have been successfully implemented, for example in speckle correlography [22, 23, 24], to find feasible solutions to this constrained problem. These techniques can be directly applied to ghost imaging as well, provided that the transmitter SLM modulation rate is sufficiently fast relative to the atmospheric coherence time.

V. Signal-to-Noise Ratio

Now that we have established the image characteristics of the ghost imaging configuration in Figure 2, let us turn our attention to its signal-to-noise ratio. We define the SNR of each measurement as

$$\mathrm{SNR} = \frac{|\langle c_{\mathbf{n}}\rangle|^2}{\langle \Delta c_{\mathbf{n}}^2\rangle} \tag{34}$$

where $\Delta c_{\mathbf{n}} = c_{\mathbf{n}} - \langle c_{\mathbf{n}}\rangle$. Because we have already computed the numerator in equation (24), we start by evaluating the denominator. The variance of the $c_{\mathbf{n}}$ measurement can be written as

$$\langle |\Delta c_{\mathbf{n}}|^2\rangle = \frac{1}{T^2}\int_{-T/2}^{T/2}\int_{-T/2}^{T/2}\iint h_B(t_1-\tau_1)h_B(t_2-\tau_2) \times \mathrm{cov}\big(g_{\mathbf{n}}^*(t_1)i_\infty(\tau_1), g_{\mathbf{n}}(t_2)i_\infty(\tau_2)\big)\,\mathrm{d}\tau_1\mathrm{d}\tau_2\mathrm{d}t_1\mathrm{d}t_2 \tag{35}$$

where $\mathrm{cov}(X,Y) \equiv \langle XY\rangle - \langle X\rangle\langle Y\rangle$. The covariance in the integrand of equation (35) can be expanded as

$$\mathrm{cov}\big(g_{\mathbf{n}}^*(t_1)i_\infty(\tau_1), g_{\mathbf{n}}(t_2)i_\infty(\tau_2)\big) \equiv \big\langle g_{\mathbf{n}}^*(t_1)g_{\mathbf{n}}(t_2)i_\infty(\tau_1)i_\infty(\tau_2)\big\rangle - \big\langle g_{\mathbf{n}}^*(t_1)\langle i_\infty(\tau_1)|\{f_{\mathbf{n}}\}\rangle\big\rangle\big\langle g_{\mathbf{n}}(t_2)\langle i_\infty(\tau_2)|\{f_{\mathbf{n}}\}\rangle\big\rangle\,. \tag{36}$$

The first term in this covariance can be evaluated as

$$\begin{aligned}\langle g_{\mathbf{n}}^*(t_1)g_{\mathbf{n}}(t_2)i_\infty(\tau_1)i_\infty(\tau_2)\rangle &= \big\langle g_{\mathbf{n}}^*(t_1)g_{\mathbf{n}}(t_2)\langle i_\infty(\tau_1)i_\infty(\tau_2)|\{f_{\mathbf{n}}\}\rangle\big\rangle \\ &= \Big\langle g_{\mathbf{n}}^*(t_1)g_{\mathbf{n}}(t_2)\Big[\big\langle \Delta i_\infty(\tau_1)\Delta i_\infty(\tau_2)|P(\cdot),\{f_{\mathbf{n}}\}\big\rangle \\ &\qquad + \big\langle i_\infty(\tau_1)|P(\cdot),\{f_{\mathbf{n}}\}\big\rangle\big\langle i_\infty(\tau_2)|P(\cdot),\{f_{\mathbf{n}}\}\big\rangle\Big]\Big\rangle\,.\end{aligned} \tag{37}$$

We substitute the conditional mean from equation (16) and the conditional covariance from equation (17) into equation (37) above, to arrive at the following expression for the conditional correlation of the (infinite-bandwidth) photocurents:

$$\begin{aligned}&\langle i_\infty(\tau_1)i_\infty(\tau_2)|\{f_{\mathbf{n}}\}\rangle \\ &\quad = \Big[FG^2\big(\eta\langle P(\tau_1)|\{f_{\mathbf{n}}\}\rangle + \lambda_d + N_T\big)\Big]\delta(\tau_1-\tau_2) + G^2\eta^2\langle P(\tau_1)P(\tau_2)|\{f_{\mathbf{n}}\}\rangle + K_1\end{aligned} \tag{38}$$

where we have not bothered to express K_1 explicitly, as it represents the terms that will be filtered out by the DC notch in the $h_R(t)$ filter. To evaluate equation (38) we must first evaluate the conditional correlation function of $P(t)$, using its definition from equation (18). Noting that E_2 and E_B are statistically-independent random fields, and recalling that E_B is a Gaussian random field with low spatiotemporal coherence, we can expand this correlation as

$$\langle P(\tau_1)P(\tau_2)|\{f_{\mathbf{n}}\}\rangle \cong \int_{\mathcal{A}_R}\int_{\mathcal{A}_R} \langle |E_2(\boldsymbol{\rho}_1,\tau_1)|^2|E_2(\boldsymbol{\rho}_2,\tau_2)|^2|\{f_{\mathbf{n}}\}\rangle \mathrm{d}\boldsymbol{\rho}_1\mathrm{d}\boldsymbol{\rho}_2 + K_2 \tag{39}$$

where, once again, we have not bothered to evaluate K_2, which represents terms that will be filtered out by the DC notch in $h_R(t)$. Note that the fourth-order (conditional) field moment in equation (39) cannot be factored into second-order moments using the Gaussian moment factoring theorem, as $E_2(\boldsymbol{\rho},t)$ is *not* a Gaussian random field, due to the quasi-Lambertian scattering and the propagation through atmospheric turbulence. Instead, to arrive at the final expression we use equations (8) and (11), and the assumption that $T(\boldsymbol{\rho})$ is Gaussian, to express $E_2(\boldsymbol{\rho},t)$ in terms of $E_1(\boldsymbol{\rho},t)$, $\mathcal{T}(\boldsymbol{\rho})$ and the free-space propagation Green's function. To simplify the calculations into an analytically tractable form, we also assume that the object lies within a single isoplanatic patch. The details of this derivation are provided in the Appendix.

We now return to the second term in the covariance expression given in equation (36), and note that it can be evaluated as

$$\langle g^*_{\mathbf{n}}(t_1)i_\infty(\tau_1)\rangle\langle g_{\mathbf{n}}(t_2)i_\infty(\tau_2)\rangle = G^2\eta^2\langle g^*_{\mathbf{n}}(t_1)P_2(t)\rangle\langle g^*_{\mathbf{n}}(t_1)P_2(t)\rangle \tag{40}$$

where we have defined

$$P_2(t) \equiv \int_{\mathcal{A}_R} \langle |E_2(\boldsymbol{\rho},t)|^2|\{f_{\mathbf{n}}\}\rangle \mathrm{d}\boldsymbol{\rho} \tag{41}$$

for convenience. Using equations (39) and (40), we finally arrive at the following expression for the covariance function specified in equation (36):

$$\begin{aligned}
&\mathrm{cov}\big(g^*_{\mathbf{n}}(t_1)i_\infty(\tau_1), g_{\mathbf{n}}(t_2)i_\infty(\tau_2)\big) \approx \\
&\quad\Big[FG^2\eta\big\langle g^*_{\mathbf{n}}(t_1)g_{\mathbf{n}}(t_2)P_2(\tau_1)\big\rangle + \langle g^*_{\mathbf{n}}(t_1)g_{\mathbf{n}}(t_2)\rangle\Big\{FG^2\big(\eta I_B A_R + \lambda_d\big) + N_T\Big\}\Big]\delta(\tau_1-\tau_2) \\
&\qquad + G^2\eta^2\big\langle g^*_{\mathbf{n}}(t_1)g_{\mathbf{n}}(t_2)\langle P_2(\tau_1)P_2(\tau_2)|\{f_{\mathbf{n}}\}\rangle\big\rangle - G^2\eta^2\langle g^*_{\mathbf{n}}(t_1)P_2(t)\rangle\langle g^*_{\mathbf{n}}(t_1)P_2(t)\rangle\,.
\end{aligned} \tag{42}$$

The first term in this covariance expression is nonstationary white noise resulting from beating between the modulation and the signal-generated shot noise, the background-generated shot noise, the dark noise, and the thermal noise. The second and third terms represent the excess noise resulting from the transmitter-induced intensity fluctuations via modulation.

The final step to evaluating the SNR is to substitute equation (42) into equation (35), evaluate the temporal integrals, and then substitute the result into the denominator of equation (34). We will not go into the detailed derivations in this article, as, aside from being tedious, the process is straightforward. In the limit that the detector bandwidth has

broad enough bandwidth to track the source modulations, i.e., $\omega_R T_0 \gg 1$, the SNR simplifies to

$$\mathrm{SNR} = \frac{T|\widetilde{\mathcal{T}}_{\mathbf{n}}|^2 e^{-D(\mathbf{n})}}{TD_1 + T_0 D_2 + D_3} \tag{43}$$

where the three terms in the denominator of this expression are given by

$$D_1 \equiv \frac{\Omega_S}{\Omega_R}\epsilon_0 + |\widetilde{\mathcal{T}}_{\mathbf{n}}|^2(1 - e^{-D(\mathbf{n})}) \tag{44}$$

$$D_2 \equiv \sqrt{\frac{\pi}{2}}\epsilon_1 \text{ and} \tag{45}$$

$$D_3 \equiv \frac{1}{\kappa^2}[2FG\kappa\widetilde{\mathcal{T}}_{\mathbf{0}} + FG^2\eta I_B A_R + FG^2\lambda_d + N_T]\,. \tag{46}$$

In equations (43)–(46)

$$\epsilon_0 \equiv \frac{1}{(2M+1)^2}\sum_{\mathbf{n}} |\widetilde{\mathcal{T}}_{\mathbf{n}}|^2 \tag{47}$$

is the square-averaged return from the target and $\epsilon_1 \equiv (2M+1)^4\epsilon_0(1 + \frac{\Omega_S}{\Omega_R})$, $\kappa \equiv \frac{2\eta G P d^2}{D^2}\frac{d^2}{\lambda^2 L_1^2}\frac{\Omega_R}{2\pi}$ is the mean photocurrent arising from a $\mathcal{T}(\boldsymbol{\rho}) = 1$ target, and $\widetilde{\mathcal{T}}_{\mathbf{n}}$ is defined in equation (25). When $D(\mathbf{n}) \ll 1$, such that turbulence does not impact the measurement, the SNR saturates—with a long enough integration time T—to a finite value (i.e., its maximum at the limit of fully-developed speckle), given by

$$\mathrm{SNR}_{\max} = \frac{\Omega_R}{\Omega_S} \times \frac{|\widetilde{\mathcal{T}}_{\mathbf{n}}|^2}{\sum_{\mathbf{n}} |\widetilde{\mathcal{T}}_{\mathbf{n}}|^2/(2M+1)^2}\,. \tag{48}$$

In words, the maximum SNR, in the limit of fully-developed speckle, is given by the product of two ratios: the ratio of the angular extent of the receiver to that of the transmitter as seen from the target, and the ratio of the energy in the spatial frequency component being measured to the average energy over all spatial frequencies that are measured. Consequently, much like other speckle-based imaging schemes, ghost imaging has a speckle-induced SNR limit. In particular, the target-induced speckle will saturate the SNR without any further modifications to suppress this speckle noise.

The SNR expression in equation (48) depends on the ratio of the angular extent of the receiver and transmitter, as seen by the target. This ratio's appearance in the SNR has an intuitive interpretation. Quasi-Lambertian scattering from the target surface spreads the incident energy equally over all plane-wave components in 2π steradians, with a small but nonzero coherence angle between nearby plane waves. As the receiver subtends a larger solid angle two effects are observed. First the fraction of the scattered energy collected by the receiver increases, but the effect of this on SNR is limited as the SNR of fully-developed speckle cannot be improved by increasing the signal energy. The second and more critical impact is that when Ω_R exceeds the coherence angle of the target-scattered field, independent target-induced speckles are *spatially* averaged over the bucket-detector surface, resulting in the SNR increase predicted in equation (48). This also implies that multiple bucket detectors can be utilized at the receiver (for example with a small-dimensional array) to improve the SNR in the limit of fully-developed speckle. The solid angle subtended by the illumination source, on the other hand, has the

opposite effect on the SNR. Recall that when operating in the diffraction-limited regime, the source-generated speckle pattern on the target surface is inversely proportional to Ω_S, i.e., as Ω_S increases, smaller speckles are generated on the target surface, which results in higher resolution. However, as the speckle size shrinks, each resolution cell averages over a smaller scattering surface area, resulting in larger fluctuations in the returned photons and a corresponding reduction in the image SNR.

VI. Discussion

Ghost imaging is an emerging imaging modality that has attracted the attention of a wide range of researchers in disciplines encompassing physics, electrical engineering, and optical engineering. Over the span of almost two decades since its first demonstration with a quantum source generating pairs of entangled photons (biphotons), ghost imaging has also been demonstrated with classical illumination sources; it has been shown to have intimate connections with speckle-based interferometry and imaging; it has been demonstrated to work with novel classical light fields such as phase-sensitive light; it has been proposed and demonstrated as a structured-illumination computational camera; and it has served as a testbed for novel image reconstruction algorithms including compressive imaging [6]. In recent years, the focus of the technical community has shifted towards determining application areas that could benefit from ghost imaging. In that vein limited results are known to date. Ghost imaging has been proposed for encryption [25], and stand-off sensing has been studied [13]. In very recent work, ghost imaging has been proposed for light detection and laser ranging (LIDAR) applications.

In this article we have focused on a ghost-imaging remote sensing architecture and have provided a rigorous treatment of its performance. Similar to previous work, we have considered turbulence in both the forward and return path, as well as the impact of diffuse surface scattering off of rough targets. However, in addition, we have included practical receiver limitations, including background radiation, sub-unity detection efficiency, dark noise, random internal gain and thermal noise. Using this framework, we have derived the mean image signature, and the SNR of the remote sensing architecture shown in Figure 2. We have also shown how speckle correlography can be applied to suppress turbulence-induced speckle.

The computational ghost imaging architecture studied in this article is a low-spatial-coherence imager: the transmitter, by use of a spatial light modulator, projects a spatiotemporally-varying speckle pattern on the target. The scattered light from the target is collected with a simple bucket detector offering no spatial resolution. The target is spatially resolved in post-processing. In its conventional form this information is obtained by correlating the temporal fluctuations of each speckle cell (which is known to the transmitter), with the aggregate photon-flux measurement, such that the average surface reflection from each speckle cell can be estimated. Although this process is straightforward in principle, the remote-sensing environment is riddled with speckle-inducing phenomena that has the potential to interfere with the operating principles of a ghost imager. Recent

work on this subject and this article show that the impact varies with the cause. First, the atmospheric turbulence on the target return path has little to no effect on the image resolution and SNR. The impact of atmospheric turbulence in the forward path depends on where the turbulence is concentrated. In particular, turbulence near the transmitter aperture is most devastating, as any aperture larger than the atmospheric coherence length provides no additional resolution. On the other hand, turbulence near the target has negligible impact on ghost imaging. The most restrictive source of speckle in remote sensing is that induced by the diffuse surface scattering from the target itself. It is evident from earlier analysis and ours that once the speckle is fully developed no additional SNR improvement is achieved with integration, and decorrelated target speckles must be obtained by using angular, spectral or polarization diversity.

To highlight the differences between conventional active imagers and ghost imaging, let us briefly compare the Figure 2 ghost imager to a conventional laser radar imager using a flood-light illumination source, as shown in Figure 6. This comparison has been addressed in earlier publications, but we shall offer some additional insights not noted elsewhere. It is well-known that the laser radar scheme shown in Figure 6 achieves a resolution limit that is very similar to that derived earlier for ghost imaging (see equation (30)), namely the resolution is given by

$$r_{\mathrm{lr}} = \frac{2\lambda_0 L_2}{D}\sqrt{1+\frac{D_R^2}{4\rho_R^2}} \tag{49}$$

where D_R is the diameter of the receiver pupil, and ρ_R is the *receiver-plane* coherence length of atmospheric turbulence on the return path to the target. Herein lies the fundamental difference between the origin of the turbulence-degradation seen in ghost imaging and flood-illumination laser-radar imaging. Whereas the ghost-imaging resolution is determined by the transmitter-plane atmospheric coherence length and otherwise is insensitive to turbulence on the return path, the flood-illumination laser-radar resolution is determined by the receiver-plane atmospheric coherence length, and otherwise is insensitive to turbulence on the forward path.[11] For horizontal-path imaging, in which the C_n^2 turbulence profile is constant over the propagation path, or in monostatic imaging configurations (i.e., when transmitter and receiver are co-located) the transmitter-plane and receiver-plane coherence lengths are equal, thus making this distinction inconsequential. However, the differences between the two schemes are highlighted when the symmetry in the imaging system is broken. As an example, consider a bistatic imaging configuration wherein the active illumination source is in Earth orbit. In this case turbulence at the transmitter is not present (specifically, the transmitter-plane coherence length ρ_0 is on the order of meters). In addition, assume that the receiver is on the ground, where turbulence is present. The Figure 2 ghost-imaging configuration is insensitive to the turbulence on the return path, and therefore attains near-diffraction-limited performance. On the other hand, the image resolution obtained from the flood-illuminating laser radar will be degraded by the return-path turbulence. Of

[11] Note that raster-scanning laser radar shares the same limitations with ghost imaging regarding forward-path turbulence. For the receive path, the sensitivity to turbulence is a function of whether the receiver performs spatially-resolved imaging.

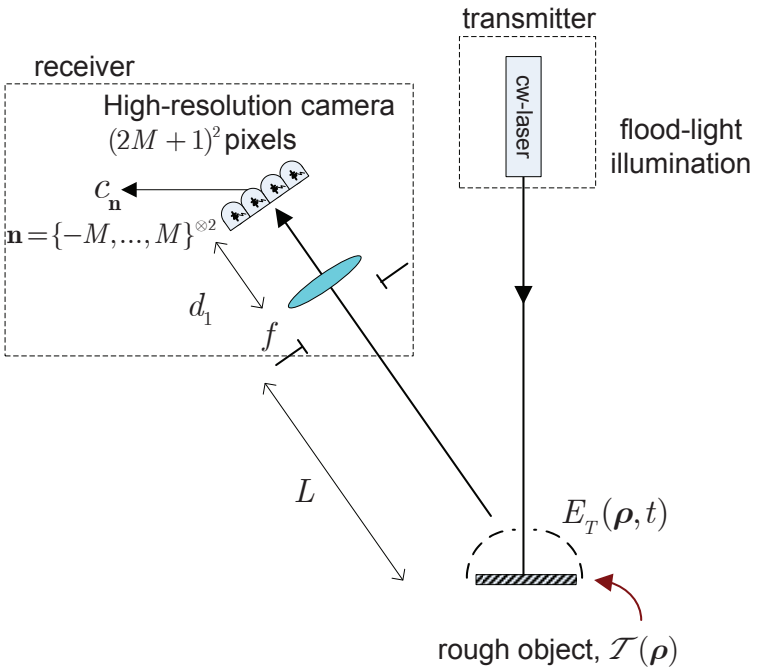

Figure 6. A generic laser radar imager that uses flood-light active illumination.

course, in the opposite scenario wherein the illumination source is on the ground and the receiver is in Earth orbit, the laser radar attains near-diffraction-limited performance whereas ghost imaging is impacted by the turbulence coherence length at the transmitter plane. Let us conclude this discussion by noting that bistatic imaging configurations have been proposed for various purposes in the literature. For example, imaging the aerosol profile of the atmosphere can be accomplished by a transmitter that focuses a laser beam to a particular layer of the atmosphere, and a receiver that is placed off to the side images the scattered light to derive an estimate of the aerosol concentration [26].

As a final point of comparison between the imaging scheme in Figure 6 and ghost imaging, let us consider their SNRs. The flood-illuminated laser radar has the well-known SNR ceiling of unity in the regime of fully-developed target-induced speckle [13]. In contrast, in ghost imaging the SNR could be greater or less than one, depending on the ratio of the solid angles subtended by the receiver and the transmitter, and the ratio of the energy in the Fourier component that is being measured and the average energy. In the bistatic configurations discussed above, large ground apertures (e.g., telescopes) are feasible, rendering potentially a larger SNR than what would be obtained with a flood-light laser radar. However, the gains in either imaging modality are severely limited by target-induced speckle noise, so any practical imager would likely employ speckle suppression algorithms to improve image quality.

Before closing our article, let us note several application areas in which ghost imaging may be desirable. In recent literature a multiple-aperture imager, which measures the far-field

speckle pattern generated from a laser beam scattering off of a target of interest has been proposed [23]. In that architecture, the target is illuminated with laser light, and the far-field speckle pattern is detected with multiple distributed apertures. Then, an iterative phase retrieval algorithm is used to estimate the transverse profile of the target. The ghost imaging architecture studied herein could be applied to the same scenario. In particular, instead of flood illuminating a target with laser light, the transmitter could generate a known time-varying speckle pattern on the region-of-interest, which eliminates the need for a spatially-resolving detector at the receiver. Furthermore, distributed apertures could be utilized to suppress target-induced speckle. Ghost imaging is also desirable for distributed imaging applications. For example, because co-location of the transmitter and receiver is not required and the receiver is very low complexity, the ghost-imaging architecture is conducive to having a single high-complexity transmitter, and multiple very low cost receivers scattered throughout a region of interest. Finally, ghost imaging may permit imaging at electromagnetic frequencies for which single-pixel detectors are feasible, but detector arrays have yet to be developed, such as the terahertz spectral range [27, 28]. Even in the infrared regime, where large arrays of photon-counting photodetectors are not yet cost effective, a small array can be paired with a multi-megapixel SLM transmitter to achieve resolutions far beyond what is achievable with the photon-counting arrays alone *and* at the ultimate quantum mechanical sensitivities afforded by the photon counters.

In summary, we have provided a thorough analysis of the performance of a ghost imaging architecture suitable for remote sensing. We have derived the image signature and SNR in the presence of turbulence, background radiation and practical photodetector noises. We have identified that turbulence which is concentrated near the transmitter aperture has the most significant impact to the attainable resolution, whereas turbulence concentrated near the target plane or that along the return path has little impact. We have briefly discussed a speckle-suppression technique, namely speckle correlography, to overcome turbulence-limited resolution. We have shown that with long integration times the SNR is eventually limited by target-induced speckle noise. Finally, we have shown that the ratio of the angular extent of the receiver to that of the transmitter, as seen from the target plane, is a key parameter that determines the maximum attainable SNR in the presence of fully-developed speckle.

A. Appendix: The Photon-Flux Correlation Function

In Section V we briefly summarized the method by which we (approximately) evaluate the integral

$$\int_{\mathcal{A}_R}\int_{\mathcal{A}_R}\langle|E_2(\boldsymbol{\rho}_1,\tau_1)|^2|E_2(\boldsymbol{\rho}_2,\tau_2)|^2|\{f_{\mathbf{n}}\}\rangle \mathrm{d}\boldsymbol{\rho}_1\mathrm{d}\boldsymbol{\rho}_2 \tag{A-1}$$

in equation (39). Here we shall provide some additional details. Using equation (11)—we suppress the time delay L_2/c for convenience—and the statistical independence of the target-induced scattering process and the return-path atmosphere, we obtain

$$\begin{aligned}
&\langle|E_2(\boldsymbol{\rho}_1,\tau_1)|^2|E_2(\boldsymbol{\rho}_2,\tau_2)|^2|\{f_{\mathbf{n}}\}\rangle \\
&\quad= \frac{1}{(\lambda_0 L_2)^4}\iint\!\!\iint\Big\langle e^{\psi^*(\boldsymbol{\rho}_1,\boldsymbol{\rho}_1')+\psi(\boldsymbol{\rho}_1,\boldsymbol{\rho}_1'')\psi^*(\boldsymbol{\rho}_2,\boldsymbol{\rho}_2')+\psi(\boldsymbol{\rho}_2,\boldsymbol{\rho}_2'')}\Big\rangle\langle T^*(\boldsymbol{\rho}_1')T^*(\boldsymbol{\rho}_2')T(\boldsymbol{\rho}_1'')T(\boldsymbol{\rho}_2'')\rangle \\
&\qquad\qquad\times e^{-i2\pi\boldsymbol{\rho}_1\cdot(\boldsymbol{\rho}_1''-\boldsymbol{\rho}_1')/\lambda_0 L_2}e^{-i2\pi\boldsymbol{\rho}_2\cdot(\boldsymbol{\rho}_2''-\boldsymbol{\rho}_2')/\lambda_0 L_2} \\
&\qquad\qquad\times\left\langle E_1^*(\boldsymbol{\rho}_1',\tau_1)E_1^*(\boldsymbol{\rho}_2',\tau_2)E_1(\boldsymbol{\rho}_1'',\tau_1)E_1(\boldsymbol{\rho}_2'',\tau_2)|\{f_{\mathbf{n}}\}\right\rangle \mathrm{d}\boldsymbol{\rho}_1'\mathrm{d}\boldsymbol{\rho}_1''\mathrm{d}\boldsymbol{\rho}_2'\mathrm{d}\boldsymbol{\rho}_2''\,.
\end{aligned} \tag{A-2}$$

Now, assuming that $T(\boldsymbol{\rho})$ is a Gaussian random field allows us to use the moment-factoring theorem [7] to obtain

$$\langle T^*(\boldsymbol{\rho}_1')T^*(\boldsymbol{\rho}_2')T(\boldsymbol{\rho}_1'')T(\boldsymbol{\rho}_2'')\rangle = \mathcal{T}(\boldsymbol{\rho}_1')\mathcal{T}(\boldsymbol{\rho}_2')\Big[\delta(\boldsymbol{\rho}_1'-\boldsymbol{\rho}_1'')\delta(\boldsymbol{\rho}_2'-\boldsymbol{\rho}_2'')+\delta(\boldsymbol{\rho}_1'-\boldsymbol{\rho}_2'')\delta(\boldsymbol{\rho}_2'-\boldsymbol{\rho}_1'')\Big]. \tag{A-3}$$

In addition, we assume that the object is in a single coherence cell of the return path turbulence, such that we can approximate $\psi(\boldsymbol{\rho},\boldsymbol{\rho}')\approx\psi(\boldsymbol{\rho},\mathbf{0})$ for $\boldsymbol{\rho}'$ coordinates at which $\mathcal{T}(\boldsymbol{\rho}')$ differs appreciably from zero. We therefore find

$$\begin{aligned}
&\langle|E_2(\boldsymbol{\rho}_1,\tau_1)|^2|E_2(\boldsymbol{\rho}_2,\tau_2)|^2|\{f_{\mathbf{n}}\}\rangle \\
&\quad= \frac{1}{(\lambda_0 L_2)^4}\iint\!\!\iint\langle|e^{\psi(\boldsymbol{\rho}_1,\mathbf{0})+\psi(\boldsymbol{\rho}_2,\mathbf{0})}|^2\rangle\mathcal{T}(\boldsymbol{\rho}_1')\mathcal{T}(\boldsymbol{\rho}_2')\Big[\langle|E_1^*(\boldsymbol{\rho}_1',\tau_1)|^2|E_1(\boldsymbol{\rho}_2',\tau_2)|^2|\{f_{\mathbf{n}}\}\rangle \\
&\quad+ e^{-i2\pi(\boldsymbol{\rho}_2-\boldsymbol{\rho}_1)\cdot(\boldsymbol{\rho}_1'-\boldsymbol{\rho}_2')/\lambda_0 L_2}\left\langle E_1^*(\boldsymbol{\rho}_1',\tau_1)E_1^*(\boldsymbol{\rho}_2',\tau_2)E_1(\boldsymbol{\rho}_1',\tau_2)E_1(\boldsymbol{\rho}_2',\tau_1)|\{f_{\mathbf{n}}\}\right\rangle\Big]\mathrm{d}\boldsymbol{\rho}_1'\mathrm{d}\boldsymbol{\rho}_2'\,.
\end{aligned} \tag{A-4}$$

We approximate the ensemble average over atmospheric turbulence as

$$\langle|e^{\psi(\boldsymbol{\rho}_1,\mathbf{0})+\psi(\boldsymbol{\rho}_2,\mathbf{0})}|^2\rangle = e^{4K_{\chi,\chi}(\boldsymbol{\rho}_2-\boldsymbol{\rho}_1,\mathbf{0})}\approx 1 \tag{A-5}$$

subsequently substitute equation (A-4) into equation (A-1), and perform the integrals over the receiver aperture (i.e., over the variables $\boldsymbol{\rho}_1$ and $\boldsymbol{\rho}_2$). Finally, we assume that the Fourier transform of the receiver aperture yields a much narrower function than $\mathcal{T}(\boldsymbol{\rho}')$, such that we can approximate

$$\left|\int_{\mathcal{A}_R} e^{-i2\pi\boldsymbol{\rho}'\cdot\boldsymbol{\rho}/\lambda_0 L_1}\mathrm{d}\boldsymbol{\rho}\right|^2 \approx A_R\lambda_0^2 L_1^2\delta(\boldsymbol{\rho}')\,. \tag{A-6}$$

Following this process we arrive at the approximate expression

$$\int_{\mathcal{A}_R}\int_{\mathcal{A}_R}\langle|E_2(\boldsymbol{\rho}_1,\tau_1)|^2|E_2(\boldsymbol{\rho}_2,\tau_2)|^2|\{f_{\mathbf{n}}\}\rangle \mathrm{d}\boldsymbol{\rho}_1\mathrm{d}\boldsymbol{\rho}_2$$
$$\approx \frac{A_R^2}{\lambda_0^4 L_2^4}\Bigg[\iint \mathcal{T}(\boldsymbol{\rho}_1')\mathcal{T}(\boldsymbol{\rho}_2')\langle|E_1^*(\boldsymbol{\rho}_1',\tau_1)|^2|E_1(\boldsymbol{\rho}_2',\tau_2)|^2|\{f_{\mathbf{n}}\}\rangle \mathrm{d}\boldsymbol{\rho}_1'\mathrm{d}\boldsymbol{\rho}_2'$$
$$+\gamma\int \mathcal{T}^2(\boldsymbol{\rho}_1')\langle|E_1^*(\boldsymbol{\rho}_1',\tau_1)|^2|E_1(\boldsymbol{\rho}_1',\tau_2)|^2|\{f_{\mathbf{n}}\}\rangle \mathrm{d}\boldsymbol{\rho}_1'\Bigg] \quad \text{(A-7)}$$

where $\gamma \equiv \lambda_0^2 L_2^2/A_R$. Next, we evaluate the moments inside the integral using $E_1(\boldsymbol{\rho},t)$ from equation (8), and we assume that the object is also in a single isoplanatic patch of the forward path turbulence, such that we obtain

$$\int_{\mathcal{A}_R}\int_{\mathcal{A}_R}\langle|E_2(\boldsymbol{\rho}_1,\tau_1)|^2|E_2(\boldsymbol{\rho}_2,\tau_2)|^2|\{f_{\mathbf{n}}\}\rangle \mathrm{d}\boldsymbol{\rho}_1\mathrm{d}\boldsymbol{\rho}_2$$
$$= \left[\frac{A_R}{\lambda_0^2 L_2^2}\frac{Pd^2}{D^2}\frac{d^2}{\lambda_0^2 L_1^2}\right]^2 \sum_{\mathbf{n}_1}\sum_{\mathbf{m}_1}\sum_{\mathbf{n}_2}\sum_{\mathbf{m}_2} f_{\mathbf{n}_1}^*(\tau_1) f_{\mathbf{m}_1}(\tau_1) f_{\mathbf{n}_2}^*(\tau_2) f_{\mathbf{m}_2}(\tau_2)$$
$$\times \left\langle e^{\psi^*(\mathbf{0},\mathbf{n}_1 d)+\psi(\mathbf{0},\mathbf{m}_1 d)+\psi^*(\mathbf{0},\mathbf{n}_2 d)+\psi(\mathbf{0},\mathbf{m}_2 d)}\right\rangle \left[\widetilde{\mathcal{T}}_{\mathbf{n}_1-\mathbf{m}_1}\widetilde{\mathcal{T}}_{\mathbf{n}_2-\mathbf{m}_2}+\gamma\widetilde{\mathcal{T}}'_{\mathbf{n}_1-\mathbf{m}_1+\mathbf{n}_2-\mathbf{m}_2}\right] \quad \text{(A-8)}$$

where

$$\widetilde{\mathcal{T}}_{\mathbf{n}} \equiv \int \mathcal{T}(\boldsymbol{\rho}) e^{i2\pi d\mathbf{n}\cdot\boldsymbol{\rho}/\lambda_0 L_1}\mathrm{d}\boldsymbol{\rho} \quad \text{(A-9)}$$

as we had defined earlier in equation (25), and

$$\widetilde{\mathcal{T}}'_{\mathbf{n}} \equiv \int \mathcal{T}^2(\boldsymbol{\rho}) e^{i2\pi d\mathbf{n}\cdot\boldsymbol{\rho}/\lambda_0 L_1}\mathrm{d}\boldsymbol{\rho}\,. \quad \text{(A-10)}$$

The expression in equation (A-8) is suitable to substitute back into equation (39). The path to the final SNR expression stated in equation (43) follows a few more straightforward steps once this substitution is carried out: the expectation over all jointly-Gaussian $\{f_{\mathbf{n}}\}$ processes is evaluated using the moment-factoring theorem. This factoring results in the turbulence moment in equation (A-8) evaluating to approximately unity inside the summation. In the final steps in arriving at the final SNR expression, we use that $\widetilde{\mathcal{T}}'_{\mathbf{0}} = D^2\epsilon_0/\lambda_0^2 L_1^2$, where ϵ_0 is defined in equation (47). Note that this expression follows from the Parseval's relation between $\mathcal{T}(\boldsymbol{\rho})$ and $\widetilde{\mathcal{T}}_{\mathbf{n}}$.

References

[1] T. B. Pittman, Y. H. Shih, D. V. Strekalov, and A. V. Sergienko, "Optical Imaging by Means of Two-Photon Quantum Entanglement," *Physical Review A*, vol. 52, p. R3429, 1995.

[2] A. Gatti, E. Brambilla, M. Bache, and L. A. Lugiato, "Correlated Imaging, Quantum and Classical," *Physical Review A*, vol. 70, p. 013802, 2004.

[3] A. Gatti, E. Brambilla, M. Bache, and L. A. Lugiato, "Ghost Imaging with Thermal Light: Comparing Entanglement and Classical Correlation," *Physical Review Letters*, vol. 93, p. 093602, 2004.

[4] Y. Cai and S.-Y. Zhu, "Ghost imaging with Incoherent and Partially Coherent Light Radiation," *Physical Review E*, vol. 71, p. 056607, 2005.

[5] B. I. Erkmen and J. H. Shapiro, "Unified Theory of Ghost Imaging with Gaussian-State Light," *Physical Review A*, vol. 77, p. 043809, 2008.

[6] B. I. Erkmen and J. H. Shapiro, "Ghost Imaging: From Quantum to Classical to Computational," *Advances in Optics and Photonics*, vol. 2, pp. 404–450, 2010.

[7] L. Mandel and E. Wolf, *Optical Coherence and Quantum Optics*. Cambridge: Cambridge Univ., 1995.

[8] J. H. Shapiro, "Computational Ghost Imaging," *Physical Review A*, vol. 78, p. 061802(R), 2008.

[9] Y. Bromberg, O. Katz, and Y. Silberberg, "Ghost Imaging with a Single Detector," *Physical Review A*, vol. 79, p. 053840, 2009.

[10] P. K. Baheti and M. A. Neifeld, "Feature-Specific Structured Imaging," *Applied Optics*, vol. 45, pp. 7382–7391, 2006.

[11] O. Katz, Y. Bromberg, and Y. Silberberg, "Compressive Ghost Imaging," *Applied Physics Letters*, vol. 95, p. 131111, 2009.

[12] R. Meyers and K. S. Deacon, "Quantum Ghost Imaging Experiments at ARL," *Proceedings of the SPIE*, vol. 7815, p. 78150I, 2010.

[13] N. D. Hardy and J. H. Shapiro, "Ghost Imaging in Reflection: Resolution, Contrast, and Signal-to-Noise Ratio," *Proceedings of the SPIE*, vol. 7815, p. 78150L, 2010.

[14] J. Cheng, "Ghost Imaging Through Turbulent Atmosphere," *Optics Express*, vol. 17, pp. 7916–7921, 2009.

[15] N. M. Hardy, *Analyzing and Improving Image Quality in Reflective Ghost Imaging*. PhD thesis, Massachusetts Institute of Technology, Cambridge, MA, 2011.

[16] R. F. Lutomirski and H. T. Yura, "Propagation of a Finite Optical Beam in an Inhomogeneous Medium," *Applied Optics*, vol. 10, pp. 1652–1658, 1971.

[17] J. H. Shapiro, *Imaging and Optical Communication Through Atmospheric Turbulence*, ch. 6. New York, NY: Springer-Verlag, 1978.

[18] L. C. Andrews and R. L. Phillips, *Laser Beam Propagation through Random Media*. Bellingham: SPIE, 2nd ed., 2005.

[19] M. H. Lee, J. F. Holmes, and J. R. Kerr, "Statistics of Speckle Propagation Through the Turbulent Atmosphere," *Journal of the Optical Society of America*, vol. 66, pp. 1164–1172, 1976.

[20] D. Kryskowski and G. H. Suits, *Sources of Radiation*, vol. 1, ch. 3. Bellingham, WA: SPIE Press, 1993.

[21] N. S. Kopeika and J. Bordogna, "Background Noise in Optical Communication Systems," in *Proceedings of the IEEE*, vol. 58, pp. 1571–1577, 1970.

[22] J. W. Goodman, *Speckle Phenomena in Optics*. Greenwood Village, CO: Ben Roberts, 2007.

[23] J. R. Fienup, "Lensless coherent imaging by phase retrieval with an illumination pattern constraint," *Optics Express*, vol. 14, pp. 498–508, 2006.

[24] P. S. Idell, J. R. Fienup, and R. S. Goodman, "Image Synthesis From Nonimaged Laser-Speckle Patterns," *Optics Letters*, vol. 12, pp. 858–860, 1987.

[25] P. Clemente, V. Durán, V. Torres-Company, E. Tajahuerce, and J. Lancis, "Optical Encryption Based on Computational Ghost Imaging," *Optics Letters*, vol. 35, pp. 2391–2393, 2010.

[26] B. M. Welsh and C. S. Gardner, "Bistatic Imaging Lidar Technique for Upper Atmospheric Studies," *Applied Optics*, vol. 28, pp. 82–88, 1989.

[27] S. Komiyama, "Single-Photon Detectors in the Terahertz Range," *IEEE Journal of Selected Topics in Quantum Electronics*, vol. 17, pp. 54–66, 2011.

[28] M. J. Fitch and R. Osiander, "Terahertz Waves for Communications and Sensing," in *Johns Hopkins APL Technical Digest*, vol. 25, pp. 348–355, 2004.